# LANGMUIR

pubs.acs.org/Langmuir Article

# Subphase Exchange Cell for Studying Fluid—Fluid Interfaces with Optical Microscopy

Benjamin A. Appleby, Amy Chacon, Arpit Mishra, Matteo Liserre, David M. Goggin, and Joseph R. Samaniuk\*



Cite This: Langmuir 2024, 40, 2174-2182



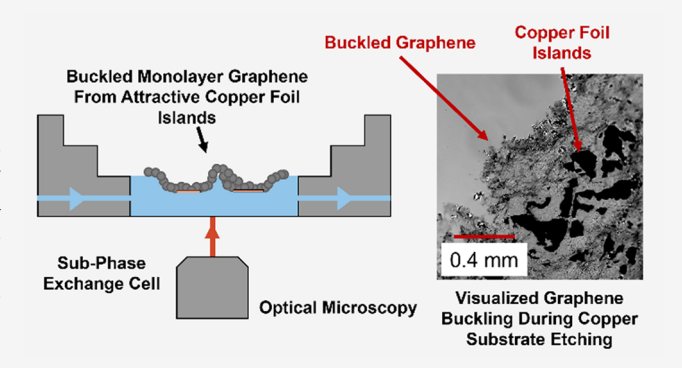
**ACCESS** I

III Metrics & More

Article Recommendations

s) Supporting Information

ABSTRACT: A subphase exchange cell was designed to observe fluid—fluid interfaces with a conventional optical microscope while simultaneously changing the subphase chemistry. Materials including phospholipids, asphaltenes, and nanoparticles at fluid—fluid interfaces exhibit unique morphological changes as a function of the bulk-phase chemistry. These changes can affect their interfacial material properties and, ultimately, the emergent bulk material properties of the films, foams, and emulsions produced from such interfacial systems. In this work, we combine experiments, computational fluid dynamics simulations, and modeling to establish the operating parameters for a subphase exchange cell of this type to reach a desired concentration. We used the experimental setup to investigate changes to a graphene



film during a common wet-etching transfer process. Observations reveal that capillary interactions can induce defects and deformations in the graphene film during the wet-etching process, an important finding that must be considered for any wet-etching transfer technique for 2D materials. More generally, conventional optical microscopy was shown to be able to image the dynamics of interfacial systems during a bulk-phase chemistry change. Potential applications for this equipment and technique include observing morphological dynamics of phospholipid film structure with subphase salinity, asphaltene film structure with subphase pH, and particle film synthesis with subphase chemistry.

#### ■ INTRODUCTION

The application of this work is on the reaction and release of material at a fluid-fluid interface, and the method presented here can be broadly applicable to fluid-fluid interface systems. Fluid-fluid interfaces are critical components of many bulk materials such as foams and emulsions, and they are important parts of facilitating many dynamic processes such as multiphase polymerization, oil and gas separations, and biological respiration.<sup>3</sup> Properties of complex fluid-fluid interfaces such as the surface tension, the interfacial rheology, and the interfacial morphology influence bulk materials properties like emulsion, foam, and film stability.4-6 It is also known that changes in bulk-phase chemistry or composition often occur in such systems, and those changes can significantly alter film interfacial properties. 7,8 The simplest examples are changes to interfacial tension due to changes in bulk-phase salinity,9 or bulk-phase concentration of a soluble surfactant. 10 In oil and gas recovery, naturally occurring surface-active compounds called asphaltenes form films that stabilize oil and water emulsions, the interfacial properties of which can be altered with changes to bulk-phase pH. 11,12 In pharmaceutical applications, the structure of proteins at fluid-fluid interfaces is particularly important due to the tendency of interfacially

trapped proteins to denature. <sup>13–15</sup> In biology, phospholipid films at fluid–fluid interfaces are ubiquitous and have been extensively studied to understand the structures that form in bilayer and monolayer membranes. <sup>16,17</sup> The stability of such films is dependent on bulk-phase pH and salinity. <sup>18,19</sup> Systems of particles trapped at fluid–fluid interfaces can be made to form films on solid substrates, or made to form Pickering emulsions, and bulk-phase composition such as pH and salinity can change interparticle interactions that impact optical properties or emulsion stability. <sup>20</sup>

Although we know bulk-phase composition is coupled with interfacial properties, we have little understanding of the dynamics of such changes in most systems with complex fluid—fluid interfaces. The study of the dynamics of molecules and particles at fluid—fluid interfaces encompasses a wide range of applications, but fluid—fluid interfaces are also important in

Received: October 17, 2023 Revised: December 19, 2023 Accepted: December 20, 2023 Published: January 16, 2024





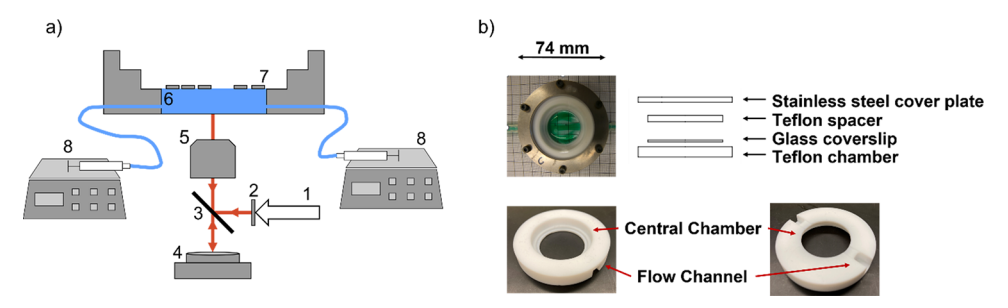


Figure 1. Subphase exchange cell illustration, drawings, and physical setup. (a) Illustration of the subphase exchange cell with an inverted microscope and synchronized syringe pumps. Number labels indicate (1) the epifluorescent light source, (2) a wavelength filter, (3) a 50/50 beam splitter, (4) the camera, (5) the objective, (6) the subphase, (7) the interface, and the (8) syringe pumps. From left to right and top to bottom, (b) a top-down image of the assembled exchange cell and exploded drawing (top right—side view) of the exchange cell showing the four main components; the bottom figures are the Teflon spacer, the left figure is the same orientation as the top-down image, and the right figure is the same spacer flipped upside down. The central chamber and reducing in and out flow channels are highlighted by the red arrows. These are both negative spaces where fluid will run through the flow channels and into the central chamber, but no material is present in the current image.

reactive systems such as polyester production via interfacial polymerization or the transfer of two-dimensional (2D) material films. For example, graphene is often grown on copper foil using chemical vapor deposition, and then transferred to other substrates by placing the foil at an airaqueous interface of ammonium persulfate (APS).<sup>21</sup> Persulfate oxidizes copper metal to soluble copper sulfate, and in the context of 2D material transfer, the process is referred to as wet etching.<sup>22</sup> The remaining graphene film at the fluid-fluid interface is then deposited on a preferred substrate. Transferring 2D materials from one substrate to another without significant damage to the 2D material itself is an active research area with challenges that remain.<sup>23</sup> This work focuses on the reaction of copper foil with APS to release graphene to a fluidfluid interface, and the method presented will be broadly applicable to emulsion, foam, and film systems as well.

Although it is known that changes in bulk-phase composition lead to changes in interfacial properties in a variety of systems, there are few studies aimed at understanding such dynamics. This is due in part to the challenge of altering the bulk-phase composition in a controlled way, without disturbing the interface, while simultaneously investigating the film properties of interest. There are a few studies that have provided data in such systems where the bulk-phase chemistry has been changed while interfacial properties were monitored. A pendant drop device has been used for this purpose, where two concentric capillaries can be arranged such that fluid injected through the inner capillary can be withdrawn through the annular space between the capillaries without changing droplet volume. 10 Wege et al. 10 used this technique to investigate changes in the solubility of the surfactant dimyristoylphosphatidyl choline (DMPC) after exchanging the subphase with a solution of pancreatic phospholipase A2 (PLA<sub>2</sub>), which hydrolyzes the DMPC and increases its solubility in the bulk phase. Although this technique works well for measuring dynamic changes in surface tension at constant surface area or changes in droplet surface area at constant surface tension, other interfacial properties such as interfacial shear rheology or interfacial morphology require different experimental equipment. Rühs et al. measured changes in the interfacial shear rheology of b-lactoglobulin fibril at oil-water interfaces during changes in pH and ionic strength using a bicone geometry. They found that the interfacial moduli were a strong function of both pH and ionic strength. Their exchange cell utilized simultaneous injection

and withdrawal of fluid into the cell utilizing synchronized syringe pumps, and they incorporated a peristaltic pump to generate a continuous flow within the subphase to encourage mixing. Their work showed how interfacial rheology can change significantly with bulk-phase composition changes, but they did not investigate the influence of mixing dynamics within the subphase. Schroyen et al. used a double-wall ring geometry<sup>24</sup> to measure the interfacial rheology of colloidal particles subject to changes in bulk-phase electrolyte concentration, and proteins subject to changes in bulk-phase pH. They used computation fluid dynamics (CFD) simulations to understand how the design of the custom double-wall geometry, with its multiple injection and withdraw ports, influenced the nature of flow and mixing during an exchange. They also performed experiments utilizing UV-vis, conductivity, and fluorescence to confirm the average exchange cell concentrations and validate the CFD results. Their work established that the design of an exchange cell, especially the injection and withdrawal port locations, will influence the dynamics of subphase composition.

The studies discussed in the previous paragraph are examples of successful integration of bulk-phase exchange with measurements of interfacial properties of interest, but methods for combining microscopy with bulk-phase exchange are lacking. The ability to observe changes in interfacial morphology during and after changes in bulk-phase composition is important because the structure of complex fluid-fluid interfaces is tightly connected with film properties, especially rheology.<sup>25</sup> The lack of studies in this area is due, in part, to the difficulty of performing simultaneous microscopy and controlled bulk-phase exchange. The challenge is to integrate three independent systems: a custom Langmuir trough, a set of pumps to perform an exchange, and a microscope to visualize the interfacial area within the trough. Integrating these in an arrangement that provides a stable interface even during the steady flow of bulk-phase fluid during an exchange while also maintaining high-image resolution is the challenge that we address in the work that follows (interface stability is addressed in detail in Supporting Information B). We have developed a simple assembly and a methodology for executing a controlled change in the bulkphase composition while observing the interface with microscopy during and after the exchange. We combine experiment, theory, and CFD simulations to understand when a particular bulk-phase composition has been achieved. The

first-order dynamics model developed and validated in the work here is generalizable to other subphase exchange cell designs, and therefore, the methodology is of broader value to other exchange cell designs that may be integrated into other microscopy setups. Finally, we test our original subphase exchange cell with a wet-etching process typically used to transfer graphene from its growth substrate to another substrate and discover that capillary interactions buckle graphene film during wet etching.

#### EXPERIMENTAL SECTION

A subphase exchange cell allows for the chemistry of one or more of the bulk phases around a fluid-fluid interface to be altered with a pair of synchronized syringe pumps without disturbing the interfacial material. Avoiding interfacial disturbances is a critical concern when interfacial structure is important, such as in interfacial rheological measurements.<sup>8</sup> Wet-etching processes have the added advantage that samples do not need to be transferred by hand, reducing the chances of damaging the sample in transfer. A subphase exchange cell designed for microscopy also needs to allow visualization of the interface and minimize drift of the interface through the field of view. This was accomplished by designing an exchange cell with injection and withdraw ports, inspired by the microscopy chambers described by Blair<sup>26</sup> and Kale et al.<sup>27</sup> Figure 1 includes illustrations and images of the subphase exchange cell used in this work. Figure 1a shows how a single inlet port and a single outlet port are used by a pair of synchronized syringe pumps (one injects while the other withdraws at the same rate) to perform an exchange. Based on the green tracer dye experiments in Figure 2 and the CFD simulations in Figure 3, a front

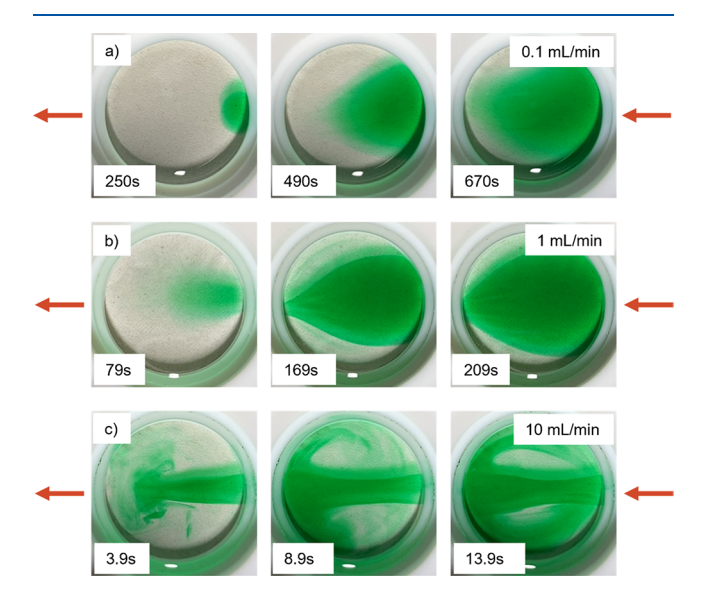


**Figure 2.** Green tracer dye is used to visualize flow patterns in the subphase during an exchange in the exchange cell. Each row represents a specified flow rate with each image representing a different point in time: (a) 0.1 mL/min, (b) 1 mL/min, and (c) 10 mL/min. Time 0 s is defined as the instant tracer die enters the cell from the right, consistent with the definition used in **Figure 3**. The exchange cell diameter is 30 mm across.

of concentrated fluid will flow from the inlet to the outlet port at opposite ends of the subphase exchange cell so the fastest removal of low-concentration fluid from the system will be in this arrangement. The tubing used was polypropylene. In Figure 1b, the four layers of the subphase exchange cell are shown with the exploded perspectives: the base Teflon chamber, a round glass coverslip (30 mm diameter, 150  $\mu$ m thickness), a Teflon spacer, and a stainless steel cover plate. The Teflon spacer is shown in the bottom left and right with inlet and

outlet flow channels with a reducing height (1-0.5 mm tall), 6 mm wide) and a central chamber (30 mm diameter, 1.5 mm tall). All four layers are held tightly together to form a seal with the coverslip with six, 5 mm long M3 screws. The Teflon spacer has a 1.5 mm vertical step to hold a subphase liquid against the glass coverslip and contains a subphase volume of 1.06 mL when the interface is flat. An upperphase liquid (e.g., oil) can be used, but in this work, the subphase is aqueous and the upper phase is air.

The bulk-phase exchange is done by first filling the subphase exchange cell and priming the syringe pump lines with ultraclean water (18.2 m $\Omega$  resistivity from a PURELAB Chorus 1, ELGA VEOLIA). An empty 60 mL syringe is attached to the withdraw line, and a full 60 mL of the new subphase fluid is attached to the injection line. The interface to be investigated is prepared, and the subphase exchange cell is arranged on the microscope so that the interfacial material can be visualized. The bulk water phase is then exchanged by initiating a predetermined flow rate and period of time. The selection of flow rates and times will be discussed in the Results section. The two syringe pumps (Legato 180, KD Scientific) are synchronized via an electrical cable so that one pump withdraws, while the other pump injects fluid at the same rate. This is critical for maintaining the same volume of fluid and interface height in the exchange cell at all times. Once the exchange is complete, a new exchange can be performed by removing the now-full withdraw syringe and replacing it with a full syringe of the next subphase to be injected. The syringes can then be reversed to inject a new subphase and withdraw the previously injected subphase material.

For experiments involving graphene, the graphene was purchased from Graphenea Inc. (San Sebastián, Spain) on a copper foil of 18  $\mu$ m thickness. Monolayer graphene was grown by chemical vapor deposition. Removal of the copper foil from underneath graphene was accomplished by a wet-etching process at a fluid-fluid interface. The samples mounted on copper foil are placed at an air-water interface, and 0.25 M APS is introduced into the bulk water phase, initiating a reaction where persulfate reacts with copper to yield a water-soluble copper sulfate. The reaction takes approximately 2 h to visibly remove all the copper foil, leaving behind the graphene film. Commonly, the etching of copper foil by APS and washing away excess APS is accomplished by bath transfers, physically lifting and moving the foils and films to the various subphases. In this work, the change in subphase chemistry is accomplished with synchronized syringe pumps and a microscopy-capable subphase exchange cell designed with inlet and outlet ports so that film structure during wet etching can be observed while removing the need for bath transfers. Microscopy images are collected using interference reflection microscopy (IRM), an interferometric technique that provides better contrast in visualizing graphene than bright field microscopy. APS is a highly corrosive material that should be handled with care and the appropriate personal protective equipment, following the Safety Data Sheet.

Simulations were performed by using COMSOL Multiphysics. The subphase exchange cell geometry was imported from SOLIDWORKS and cut in half to have a symmetry boundary condition to reduce computational time, as seen in Figure 3a. In each of the cells of Figure 3a, flow moves from right to left at each rectangular protrusion, and all other boundaries are stationary walls with no reactions occurring, except for the symmetry boundary. The simulation is 3D and performed under Laminar Flow and with the Transport of Diluted Species package. The fluid properties used are for water, and the concentration of injected dilute species is APS with a concentration of 150 mol/m<sup>3</sup> with an assumed diffusion coefficient  $D \sim O^{9-}$  m<sup>2</sup>/s, which is reasonable for a small molecule solute in an aqueous suspension. 31,32 All surfaces have a no-slip boundary condition. The inlet flow rate was specified at 1 mL/min by specifying a normal inlet flow velocity of  $4.6 \times 10^{-4}$  m/s, and the outlet was set to atmospheric pressure. Output from the simulations includes false color images indicating concentrations of dilute species throughout the exchange cell, concentration profiles along cut lines through the exchange cell, and average exchange cell concentration as a function of time.

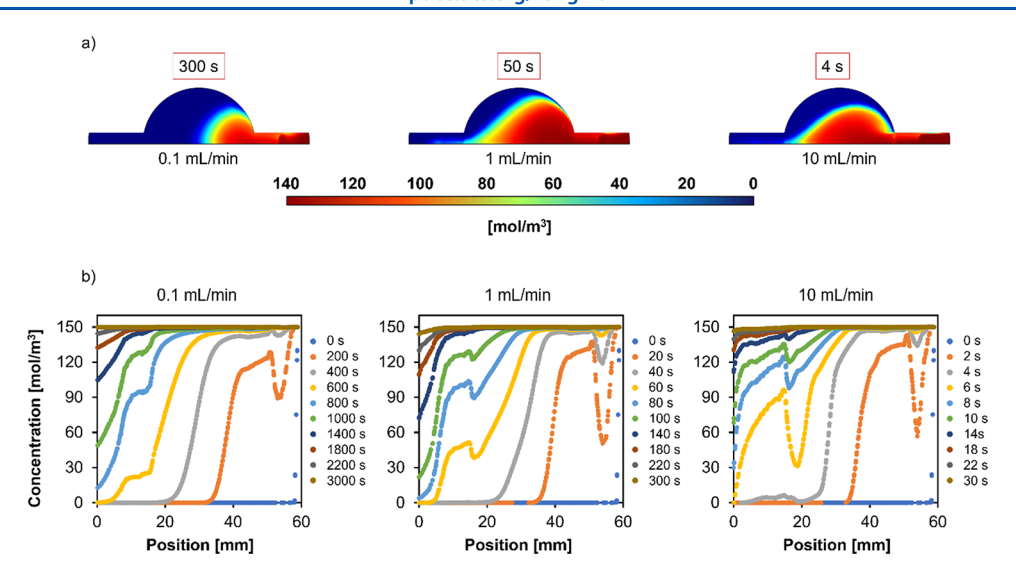


Figure 3. Simulation results for the bulk-phase exchange to determine the effects of concentration profiles on the dynamics of the total average concentration achieved in the exchange cell. (a) False colored map of concentration to show exchange evolution over time at each respective flow rate, matching those same qualitative appearances as the colored food dye experiments. The subphase exchange cell is halved along a symmetry boundary. (b) Concentration as a function of position along the bottom edge of the subphase exchange cell, representing the centerline of the subphase exchange cell setup. Concentration is tracked over the length of the exchange cell, and each trendline represents progressing points in time to track how the concentration profile changes throughout the bulk-phase exchange.

Estimates of shear stress on the interface from bulk phase flow are made and discussed in Supporting Information B.

#### RESULTS AND DISCUSSION

Design Validation. Exchanging the subphase in a controlled manner to obtain a desired concentration requires an understanding of the influence of initial concentrations, flow rate, and time. In this section, we perform experiments with tracer dye and use the results to qualitatively validate the CFD simulations that are used to establish a first-order dynamics model for subphase concentration. The tracer dye experiments are used to qualitatively determine flow rates that would be reasonable for operation and yield uniform mixing in the subphase exchange cell. The CFD simulations are used to quantitatively determine flow rates and time of exchange that will yield a full subphase exchange and wet-etch the copper foil. The extent of mixing is strongly influenced by the flow rate and location of inlet and outlet ports. The extent of mixing within the exchange cell is important for the validity of the first-order dynamics model proposed since the assumption of perfect mixing is invoked. In both the tracer dye experiments and the CFD simulations, four flow rates are investigated: 0.1 1.0, 2.0, and 10 mL/min. In all cases, we find that the first-order system assuming perfect mixing is a good predictor of the final subphase concentration after a period of time defined by the ratio of the exchange cell volume to the injection volumetric flow rate.

Tracer Dye Experiments. Mixing is a complex behavior that depends on flow rate as well as subphase exchange cell geometry. Perfect mixing is defined as the exit flow (withdraw flow) having the same concentration as that of the average concentration within the subphase exchange cell. This is an important assumption for the first-order model discussed later, but perfect mixing is never accomplished. Figure 2 reveals that the extent and even the nature of mixing in our exchange cell are a strong function of flow rate. The exchanges shown in Figure 2 were prepared as described in the Materials and Methods section, but the injected stream contained a green

tracer dye, and no interfacial material was present (i.e., it is a clean air—water interface). Flow rates of 0.1, 1, and 10 mL/min were selected to broadly capture the desired minimum and maximum flow rates to be operated at based on time and geometric constraints. For each flow rate, snapshots of the video-recorded experiment were chosen to qualitatively describe the flow profiles present. Figure 2a is the 0.1 mL/ min exchange and shows that a broad front of tracer dye moves from the injection site (left) toward the withdrawal site (right). Figure 2b is the 1 mL/min exchange at three different times, and the tracer dye front is narrowed, since convection plays a greater role over the diffusion process that tends to broaden the front. At 10 mL/min, shown in Figure 2c, convection dominates the dynamics, leading to a concentrated stream of tracer dye that travels from inlet to outlet almost directly. Tracer dye then begins recirculating back toward the injection port along the exchange cell walls. Each of these phenomena affects the dynamics of concentration profiles in the exchange cell, and ultimately, the average total concentration of the bulk phase. Higher exchange flow rates are expected to decrease the amount of time required to reach a particular concentration in the exchange cell, but it is not clear how changes in flow profiles will alter mixing and influence the average concentration within the exchange cell over time. Average subphase concentration within the exchange cell is the quantity of interest since stopping diffusion after an exchange will lead to a uniform exchange cell concentration on the order of minutes regardless of spatial variation in concentration once the exchange is stopped. Although it is challenging to obtain this information experimentally, it is relatively easy to do so with CFD simulations. In the following section, we use CFD software to simulate conditions similar to the tracer dye experiments in Figure 2 and use those results to understand deviations from the dynamics model that follows.

*CFD Simulations.* Results from the simulations provide details of the evolution of the dilute species concentration as a function of time. Outputs include false-color maps of concentration throughout the subphase exchange cell,

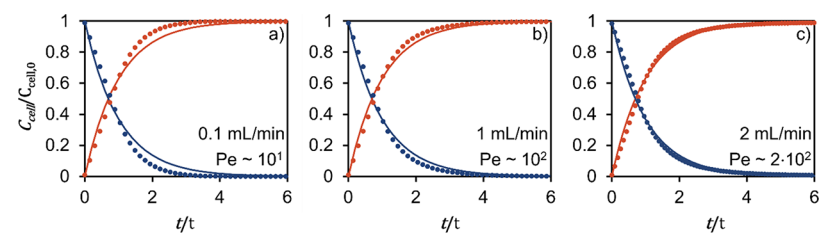


**Figure 4.** Average APS concentration in the subphase exchange cell over flow rates of (a) 0.1, (b) 1, and (c) 2 mL/min. The data points are simulation results from CFD and the trend is the first-order rate law (eq 2). The orange data is flowing in APS to an exchange cell filled with water, and the dark blue data is flowing in water to an exchange cell filled with APS. The *y*-axis is the APS concentration in the exchange cell normalized by the concentration of APS during inflow. The *x*-axis is time normalized by the time constant of each system.

concentration as a function of position along the centerline of the subphase exchange cell, and a spatially averaged concentration within the subphase exchange cell as a function of time. Figure 3a includes the false color maps of concentration for the three different volumetric flow rates, revealing dynamics similar to those shown in Figure 2, where a front of solute propagates from right to left from the injection to withdrawal line. The times and flow profiles compared between Figures 2 and 3a exhibit similar dynamics along similar times, but direct comparisons were not the intention; instead, they are to guide which flow rate for operation and which flow rates to further explore in the simulation work. Figure 3b includes the solute concentration as a function of position along the centerline of the exchange cell from right to left for each flow rate, with time as the parametric variable. The sharp fluctuations in each concentration line are indicative of complex mixing and flow profiles, especially near the exchange cell entrance and exit. This level of resolution is not available with the tracer dye experiments, but it is captured with the simulations. At the highest flow rate simulated, 10 mL/min, the false-color map does not indicate the presence of a recirculating flow, as seen in Figure 2b in the tracer dye experiments. This is likely a consequence of flow inertia in the experiments, a phenomenon not captured in the laminar flow simulations. The highest Reynold numbers for 10 mL/min simulations and experiments are on the order of 10<sup>2</sup> near the injection and withdraw ports, well below values typical for the presence of turbulence (Re >  $3.5 \times 10^3$ ), but indicative of significant flow inertia that may explain the difference in experiments and simulations at those high flow rates. Additional calculations concerning flow inertia are included in Supporting Information A. A global Peclet number can also be defined to weight the relative importance of convective mass transport to diffusive:

$$Pe = \frac{\dot{v}h}{D} \tag{1}$$

where  $\dot{\nu}$  is average flow velocity within an injection port, h is the height of the subphase fluid, and D is the solute diffusivity. An order of magnitude analysis serves to illustrate the relative importance of convective and diffusive mass transport. If a value of  $D \sim {\rm O^{9^-} \ [m^2/s]}$  is assumed,  $^{31,32}$  then for flow rates of 0.1, 1, and 10 mL/min, the Peclet numbers are on the order of  $10^1$ ,  $10^2$ , and  $10^3$ , respectively. Since the Peclet number is well above 1, convection will play the primary role in mass transport in the exchange cell rather than diffusion. In practice,  $10 \ {\rm mL/min}$  is a relatively high flow rate, it is likely to cause undesirable interfacial flows in the subphase exchange cell and should be avoided. Thus, the priority is comparing simulations and experiments at the lower flow rates of 0.1, 1, and 2 mL/

min. For our application, 2 mL/min was also a flow rate that would not affect the dynamics of our system because our materials were still mounted on the copper foil substrate during the exchange, but after the etching process if the subphase were to be altered then the effects of subphase flow on interfacial dynamics should be evaluated. Schroyen et al.<sup>8</sup> performed a nice analysis addressing convection regimes to avoid influencing material at the interface.

First-Order Dynamics Model. A first-order dynamics model is developed in this section for predicting subphase concentration with time, and the CFD simulation results serve to evaluate the validity of the model. A component mass balance is used to develop the model and can be written as

$$\frac{\mathrm{d}C_{\mathrm{cell}}}{\mathrm{d}t} = \frac{\dot{V}}{V_{\mathrm{cell}}} \cdot [C_{\mathrm{o}} - C_{\mathrm{cell}}] \tag{2}$$

Where  $C_{\rm cell}$  is the average concentration of the solute within the subphase exchange cell, t is time,  $\dot{V}$  is the injection volumetric flow rate,  $V_{\rm cell}$  is the exchange cell volume, and  $C_{\rm o}$  is the concentration of the solute in the injection flow stream. The solution of eq 2 with initial conditions of  $C_{\rm cell}/C_{\rm o}=0$  gives

$$\frac{C_{\text{cell}}}{C_{\text{o}}} = 1 - \exp\left(-\frac{t}{\tau}\right) \tag{3}$$

Where  $\tau$  is a time constant defined as  $\tau = V_{\rm cell}/\dot{V}$ . Alternatively, a solution can be developed where the subphase exchange cell initially has a nonzero solute concentration,  $C_{\rm cell,o}$ , and the injection fluid contains no solute,  $C_{\rm o} = 0$ . That solutions can be written as

$$\frac{C_{\text{cell,0}}}{C_{\text{cell,0}}} = \exp\left(-\frac{t}{\tau}\right) \tag{4}$$

Eq 3 applies when exchanging a clean solvent within the subphase exchange cell for a solution of solute and solvent in the injection fluid. eq 4 applies when the exchange cell contains a solute-solvent mixture, and the injection fluid is a clean solvent. The predictions of Eqs 3 and 4 are plotted in Figure 4 along with the average exchange cell concentrations provided by the simulations. The callouts Figure 4a, b, and c indicate the flow rates of 0.1, 1, and 2 mL/min, respectively; each set of experiments were run at the same flow concentrations. Dotted lines are the simulation results, and solid lines are theoretical predictions. Orange lines are results for the case of injecting a solute into a clean subphase exchange cell, while dark blue lines are results for the case of injecting a clean solvent into an exchange cell saturated with the solute-solvent mixture. Peclet numbers of an approximate order O<sup>1</sup>, O<sup>2</sup>, and 2 O<sup>2</sup>, as defined and discussed earlier, are shown for reference based on the simulation parameters. An important observation is that the

results agree at limits of short and long time but disagree to various extents in the range of  $0.1\tau < t < 4\tau$ , most clearly seen in Figure 4a. This is expected since perfect mixing in practice cannot be achieved, but the most important conclusion is that both results converge when  $t \ge 5\tau$ , and the exchange cell concentration reaches at least 99% of the concentration of the solute in the injection stream. This is generally expected for a system governed by first-order dynamics, but the simulation results are important for validating the length of exchange time needed to use a first-order dynamics model in a system with imperfect mixing. This conclusion is supported by the work of Schroyen et al.8 where their experimental values and simulation values lined up after enough of the subphase volume has been exchanged. The percentage of subphase volume exchanged for our system surpasses the volume need to match experimental with simulation data compared against the work of Schroyen et al.<sup>8</sup> (Supporting Information D).

The conclusion that the subphase exchange cell solute concentration can be expected to reach the injection stream solute concentration when  $t \geq 5\tau$  can be leveraged to establish minimum exchange times for a given flow rate and minimum volume requirements for the injected fluid stream. Table 1

Table 1. Operational Table to Guide Experiments for the Length of Time and Volume of APS Needed for a Bulk Fluid Exchange of the Subphase Exchange Cell<sup>a</sup>

flow rate [mL/min]	t/τ []	time [s]
0.1	5	2512
1	5	251
2	5	126

"The table outlines what real time is needed to reach 5 time constants for the minimum time needed for the subphase to reach the inlet concentration, and that time can also be used to evaluate the volume of APS needed for the exchange.

contains the time required to reach the injection stream solute concentration  $(5\tau)$  for flow rates of 0.1, 1, and 2 mL/min. The results in this table are specific to the volume of the subphase exchange cell, but the methodology described in this section can be applied to subphase exchange cells of varying volume, geometry, and design. In this way, the work described here can be generalized to other exchange cells.

Optical Interrogation of Interfacial Material. The subphase exchange cell developed here has potential applications in studying a wide range of systems where fluid-fluid interfacial structure is coupled with bulk-phase chemistry. The experiments in this section focus on the evolution of the structure of a graphene film during wet etching of the underlying copper foil substrate, a common technique used in the transfer of graphene from its growth substrate to another substrate (e.g., from copper foil to a silica wafer or TEM grid). The graphene film on copper foil is placed in the subphase exchange cell on a clean water subphase, and an exchange is initiated with the injection stream containing an aqueous solution of 0.25 M APS. In all experiments described below the volumetric flow rate of the injection and withdraw streams was 2 mL/min, and the exchange time was 176 s, 126 s of exchange to reach 5  $\tau$ , with 50 additional seconds. Etching occurs after  $5\tau$ , but refreshing the subphase concentration reduces the exchange time. The total volume of APS solution exchanged was 5.9 mL and was contained in 60 mL syringes.

The wet-etching process to solubilize the copper foil takes approximately 120 min, during which time microscopy was used to observe the nature of the etching and the influence on the remaining graphene film at the fluid—fluid interface. The etching of the copper proceeded from the edges of the film as well as from the internal area of the film. This can be seen in the images included in Figure 5a—c and d—f, where the copper

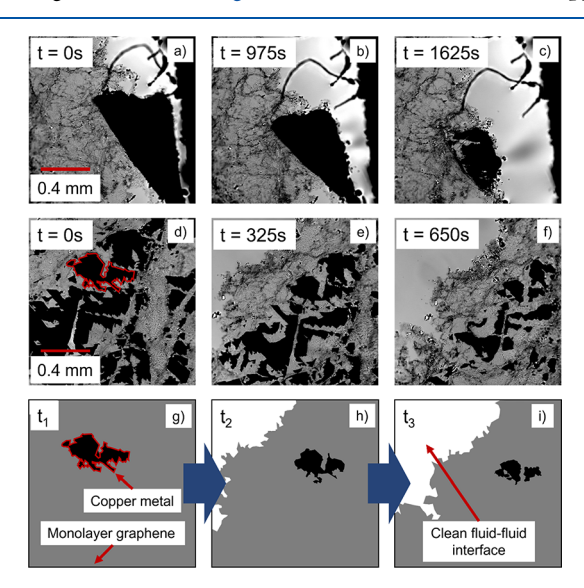


**Figure 5.** Microscopy time lapse of copper foil placed at the subphase exchange cell air—fluid interface and etched over time, leaving a film at the air-fluid interface. Images a—c and d—f use samples of graphene grown on copper, and IRM is used to visualize the graphene. Images g—i are an illustration of the copper etching process, leaving a graphene film visible by microscopy.

foil (dark black regions) appears to recede over time from the film edges as well as the film interior, and the graphene film is pulled toward the remaining copper pieces. IRM can be used to visualize graphene and identify when multiple layers of graphene are present by appearing darker. The copper foil as it etches appears like a sink where graphene film accumulates around the edge of copper pieces as it shrinks. As the copper etches, the graphene film accumulates at the edges of copper foil and becomes thicker, indicating buckling behavior. Even once the copper islands have been etched, the graphene films will remain buckled, the buckling acts as a stress relief in the system. This has been observed experimentally and shown in the literature, where the fact-to-face configuration of graphene is so energetically favorable that they will remain in that position rather than returning to lateral position.<sup>39</sup>

Two fronts are present during the reaction of copper foil to ions and the release of the graphene film to the fluid—fluid interface. A concentration front that occurs across the whole exchange cell at a short-time scale of the APS invading the subphase exchange cell that occurs over 176 s and a retreating copper front that occurs over 120 min around each piece of copper foil, shrinking and releasing graphene film.

The sporadic nature of the retreating copper front is illustrated in Figure 5d through Figure 5f, where islands of the remaining copper foil of irregular shape appear to shrink in size as they are solubilized by the APS solution. Although it is uncertain why such islands form, it is likely the consequence of submicron thickness variations in the foil such that certain regions are completely solubilized before others. A surprising



**Figure 6.** (a) Illustration of an undulated graphene film at an air—water interface with islands of copper-inducing capillary monopoles. The capillary forces and graphene rigidity resisting buckling are indicated by the material color, salmon for copper foil capillary forces and gray for monolayer graphene rigidity. (b) An illustration of stress release due to graphene film buckling and folding over to the right, with the copper foil islands closer together and smaller over the course of wet etching.

observation during the etching process is that the graphene film appears to contract between these copper foil islands, as if by buckling. This is illustrated in Figure 5g-i, which shows a time series between two of the copper islands in Figure 5d-f. The contraction of the graphene film is most evident in the video, making it clear that the film is significantly altered during the etching process. This film contraction appears to happen only between the islands of copper foil as they change shape and reduce in size over time, and it stops once all of the visible copper foil is gone. These two behaviors can potentially be explained by the presence of capillary attractions induced by the remaining islands of the copper foil. The higher density of copper foil than water, combined with copper foil islands with length scales on the order of 100  $\mu$ m, means that significant capillary monopoles are highly likely to be present despite the overlying film of graphene. When the strength of capillary attraction<sup>33-36</sup> between the copper foil islands exceeds the buckling strength of the graphene film one can expect the graphene film to experience a stress release in the form of buckling. Gradients in copper ions may be present in the solution, leading to Marangoni stresses, but they are insignificant compared to capillary forces seen by an end in buckling events once the copper foil has been etched into ions.

The hypothesis that capillary attractions of copper islands are in competition with the buckling stress of the overlying graphene film is illustrated in Figure 6. In Figure 6a, the stresses induced from bending the graphene film are in equilibrium with the capillary attractions due to the monopoles generated by the copper foil islands. In Figure 6b, the graphene film has released stress by folding to the right, and the copper foil islands have reduced in size and moved closer together.

The feasibility of the capillary-induced buckling of graphene illustrated in Figure 6 can be tested with theory by considering models for the strength of capillary attractions from monopoles and values of the critical buckling stress of a graphene monolayer. The attractive force generated by two capillary monopoles can be approximated with the relationship derived by Danov and Kralchevsky:<sup>33</sup>

$$F_{\text{capillary}}(L) \approx -2\pi\gamma q H_{\text{A}} H_{\text{B}} \frac{K_{\text{I}}(qL)}{K_{\text{0}}(qr_{\text{A}})K_{\text{0}}(qr_{\text{B}})}$$
(5)

where  $\gamma$  is surface tension, "q" is the inverted capillary length defined as  $\sqrt{\Delta \rho g/\gamma}$ , where  $\Delta \rho$  is the difference in density between the two fluids and "g" is the gravitational constant.  $H_{\rm A}$  and  $H_{\rm B}$  are the amplitudes of the out-of-plane deformation of the monopole associated with particle A and B, respectively,  $K_1$  and  $K_0$  are the modified Bessel function of the second kind of order 1 and order 0, respectively. L is the center-to-center separation distance between particles, and " $r_{\rm A}$ " and " $r_{\rm B}$ " are the radii of particles A and B, respectively. The predictions from

this model, with estimates of parameters based on experimental observations, can be compared with the critical stresses needed to buckle a graphene monolayer. The critical stress for buckling of a film can be written as

$$\sigma_{\rm CR} = \frac{\pi^2 E}{\left(\frac{L_{\rm c}}{r_{\rm x}}\right)^2} \tag{6}$$

where "E" is the elastic modulus of the film, " $L_e$ " is the effective length between the two fixed points of applied stress, and "rx" is the radius of gyration defined as  $r_x = \sqrt{I_x/A}$  where " $I_x$ " is the in-plane moment of inertia and "A" is the cross-sectional area of the film. If we assume two islands of copper foil at an air-water interface are discs of 100  $\mu$ m in diameter, with outof-plane monopole deformations of approximately 10  $\mu$ m in height, the magnitude of the capillary attractions as calculated from eq 5 is  $\sim 4 \times 10^{-8}$  N for a separation distance of 0.1 mm. The critical force for the buckling of monolayer graphene film spanning the distance between those discs would be  $\sim 1 \times$  $10^{-19}$  N based on a graphene elastic modulus of  $\sim 1.3 \times 10^5$  Pa, as calculated from literature values of graphene flexural rigidity  $\sim 1 \times 10^{-19}$  N-m.<sup>37,38</sup> The capillary force induced by the two pieces of graphene is  $4 \times 10^{-8}$  N, and the resisting force of monolayer graphene rigidity is  $\sim 1 \times 10^{-19}$  N. Capillary force exceeds the resisting force of monolayer graphene by ~ O11, showing that buckling is possible during the wet-etch process. Buckling is dependent on the attractive capillary force and geometry of the graphene film. Details of the critical buckling stress analysis are included (Supporting Information E). Although the parameters utilized (i.e., particle size, elastic modulus, separation distance) in this analysis are approximate and can vary by orders of magnitude, it is clear that forces from capillary interactions are capable of exceeding the buckling stress of a graphene film by orders of magnitude. The random nature of the appearance of islands of copper foil during the wet-etching process means that attractive capillary forces will vary in location, magnitude, and direction during etching but always act to compress the film. The capillary forces will span over 1 mm, seen in Figure S5, meaning the area of view in Figures 5 and S9 will all be experiencing capillary forces, and further stress analysis cannot be done due to the packing density and irregularities of the copper islands. Additional experiments presenting the effects of attractive interactions from capillary monopoles are in Supporting Information F.

Etching copper foil with APS is a common processing step to separate graphene from its growth substrate for transfer purposes, and the results here show that surface tension and the dynamic formation of copper foil islands can deform the graphene film significantly, leading to local buckling and compression of the original film. The findings here suggest that the transfer of graphene via APS etching of copper can be performed with an acknowledgment that the liberated film may contain multiple buckling defects. Other strategies for transfer can be invoked to maintain integrity of the film, including spin-coating a protective polymer layer (e.g., polystyrene) prior to APS etching, and then transferring the graphene film to the fluid—fluid interface by subsequent dissolution of the polymer layer with a subphase exchange of solvent (e.g., toluene or acetone).

#### CONCLUSIONS

A subphase exchange cell was designed to enable changes in bulk-phase chemistry while simultaneously visualizing interfacial structure and dynamics with optical microscopy. The flow profiles of the subphase exchange cell were explored experimentally with tracer dye, and CFD simulations were used to understand experimental results and to validate a firstorder dynamics model of the average bulk-phase concentration of an injected solute as a function of time. The operational conditions necessary to obtain a desired bulk-phase concentration for any subphase exchange were established. The device was tested by visualizing changes in graphene monolayers that occur during a typical wet-etching step to transfer graphene from a copper foil to an air-water interface, a common 2D material transfer technique, despite little being known about the influence on the 2D material structure of the wet-etching process. It was observed in these experiments that instead of a uniform removal of copper foil over time, small islands of copper foil arise intermittently with strong long-range capillary attractions between them that tend to buckle the remaining graphene film locally. These observations reveal that wetetching transfer methods for 2D materials must consider the influence of the surface tension on the remaining film structure. In particular, we found that graphene monolayers will buckle extensively during wet etching of the underlaying copper foil substrate without a protective layer. Beyond the application of 2D material transfer, we have shown that observing the structural dynamics of a fluid-fluid interface during and after a change in bulk-phase chemistry can be accomplished in a controlled way with a conventional optical microscope. The technique can be used in a wide range of investigations of interfacial systems, from understanding the influence of bulk-phase salinity on lipid monolayer structure to observing particle-particle interaction dynamics at interfaces with a changing bulk-phase pH.

## ASSOCIATED CONTENT

#### **Data Availability Statement**

The data that support the findings of this study are available within the article.

# Supporting Information

The Supporting Information is available free of charge at https://pubs.acs.org/doi/10.1021/acs.langmuir.3c03154.

Time lapse Figure 5a-c (AVI) Time lapse Figure 5d-f (AVI)

Evaluation of diffusion transport, interfacial stress contributions, profilometer data characterizing the height of photoresist material, evaluation of exchange volumes needed to reach a steady-state value matching simulations and compared against existing literature, buckling calculation details to determine capillary forces in opposition to graphene rigidity, and aggregation of

photoresist discs after etching of copper substrate to show attractive capillary forces (PDF) Time lapse Figure 5S9 (AVI)

#### AUTHOR INFORMATION

#### **Corresponding Author**

Joseph R. Samaniuk — Department of Chemical and Biological Engineering, Colorado School of Mines, Golden, Colorado 80401, United States; orcid.org/0000-0002-6077-2999; Email: samaniuk@mines.edu

#### **Authors**

Benjamin A. Appleby — Department of Chemical and Biological Engineering, Colorado School of Mines, Golden, Colorado 80401, United States; orcid.org/0000-0002-2880-2182

Amy Chacon – Department of Chemical and Biological Engineering, Colorado School of Mines, Golden, Colorado 80401, United States

Arpit Mishra — Department of Chemical and Biological Engineering, Colorado School of Mines, Golden, Colorado 80401, United States

Matteo Liserre – Department of Chemical and Biological Engineering, Colorado School of Mines, Golden, Colorado 80401, United States

David M. Goggin – Department of Chemical and Biological Engineering, Colorado School of Mines, Golden, Colorado 80401, United States

Complete contact information is available at: https://pubs.acs.org/10.1021/acs.langmuir.3c03154

#### **Author Contributions**

Performed the experiments and analyzed the data: B.A.A., A.C., and M.L. Conceived and designed experiments: B.A.A., A.C., A.M., M.L., D.M.G., and J.R.S. Prepared and synthesized graphene and photoresist samples for the wet-etching experiments: A.C. Contributed to manuscript revisions: B.A.A., A.C., A.M., M.L., D.M.G., and J.R.S. Wrote the manuscript: B.A.A. and J.R.S. All authors read and approved the final manuscript.

#### Funding

NSF Faculty Early Career Development (CAREER) Program Award CBET-1944725

#### Notes

The authors declare no competing financial interest.

# ACKNOWLEDGMENTS

We thank Manasi Vyas for careful proofreading of the manuscript. B.A.A., A.C., A.M., M.L., D.M.G., and J.R.S. acknowledge the financial support of the NSF Faculty Early Career Development (CAREER) Program Award CBET-1944725.

### REFERENCES

- (1) Zhang, F.; Fan, J.; Wang, S. Interfacial Polymerization: From Chemistry to Functional Materials. *Angew. Chem., Int. Ed.* **2020**, 59 (49), 21840–21856.
- (2) Fakher, S.; Ahdaya, M.; Elturki, M.; Imqam, A. Critical Review of Asphaltene Properties and Factors Impacting Its Stability in Crude Oil. J. Petrol. Explor. Prod. Technol. 2020, 10 (3), 1183–1200.
- (3) Veldhuizen, E. J. A.; Haagsman, H. P. Role of Pulmonary Surfactant Components in Surface Film Formation and Dynamics. *Biochim. Biophys. Acta* **2000**, 1467 (2), 255–270.

- (4) Razavi, S. M. H.; Shahmardan, M. M.; Nazari, M.; Norouzi, M. Experimental Study of the Effects of Surfactant Material and Hydrocarbon Agent on Foam Stability with the Approach of Enhanced Oil Recovery. *Colloids Surf., A* **2020**, *585*, No. 124047.
- (5) Hermans, E.; Saad Bhamla, M.; Kao, P.; Fuller, G. G.; Vermant, J. Lung Surfactants and Different Contributions to Thin Film Stability. *Soft Matter* **2015**, *11* (41), 8048–8057.
- (6) Gonzalez Ortiz, D.; Pochat-Bohatier, C.; Cambedouzou, J.; Bechelany, M.; Miele, P. Current Trends in Pickering Emulsions: Particle Morphology and Applications. *Engineering* **2020**, *6* (4), 468–482
- (7) Rühs, P. A.; Scheuble, N.; Windhab, E. J.; Mezzenga, R.; Fischer, P. Simultaneous Control of PH and Ionic Strength during Interfacial Rheology of  $\beta$ -Lactoglobulin Fibrils Adsorbed at Liquid/Liquid Interfaces. *Langmuir* **2012**, 28 (34), 12536–12543.
- (8) Schroyen, B.; Gunes, D. Z.; Vermant, J. A Versatile Subphase Exchange Cell for Interfacial Shear Rheology. *Rheol. Acta* **2017**, *56* (1), 1–10.
- (9) Nayar, K. G.; Panchanathan, D.; McKinley, G. H.; Lienhard, J. H. Surface Tension of Seawater. *J. Phys. Chem. Ref. Data* **2014**, 43 (4), No. 043103
- (10) Wege, H. A.; Holgado-Terriza, J. A.; Cabrerizo-Vílchez, M. A. Development of a Constant Surface Pressure Penetration Langmuir Balance Based on Axisymmetric Drop Shape Analysis. *J. Colloid Interface Sci.* **2002**, 249 (2), 263–273.
- (11) Poteau, S.; Argillier, J.-F.; Langevin, D.; Pincet, F.; Perez, E. Influence of PH on Stability and Dynamic Properties of Asphaltenes and Other Amphiphilic Molecules at the Oil—Water Interface. *Energy Fuels* **2005**, *19* (4), 1337—1341.
- (12) Pradilla, D.; Simon, S.; Sjöblom, J.; Samaniuk, J.; Skrzypiec, M.; Vermant, J. Sorption and Interfacial Rheology Study of Model Asphaltene Compounds. *Langmuir* **2016**, *32* (12), 2900–2911.
- (13) Sundaram, S.; Ferri, J. K.; Vollhardt, D.; Stebe, K. J. Surface Phase Behavior and Surface Tension Evolution for Lysozyme Adsorption onto Clean Interfaces and into DPPC Monolayers: Theory and Experiment. *Langmuir* 1998, 14 (5), 1208–1218.
- (14) Miller, R.; Grigoriev, D.; Kragel, J.; Makievski, A.; Maldonado-Valderrama, J.; Leser, M.; Michel, M.; Fainerman, V. Experimental Studies on the Desorption of Adsorbed Proteins from Liquid Interfaces. *Food Hydrocolloids* **2005**, *19* (3), 479–483.
- (15) Roth, S.; Murray, B. S.; Dickinson, E. Interfacial Shear Rheology of Aged and Heat-Treated  $\beta$ -Lactoglobulin Films: Displacement by Nonionic Surfactant. *J. Agric. Food Chem.* **2000**, 48 (5), 1491–1497.
- (16) Beltramo, P. J.; Van Hooghten, R.; Vermant, J. Millimeter-Area, Free Standing, Phospholipid Bilayers. *Soft Matter* **2016**, *12* (19), 4324–4331.
- (17) Kim, K.; Choi, S. Q.; Zell, Z. A.; Squires, T. M.; Zasadzinski, J. A. Effect of Cholesterol Nanodomains on Monolayer Morphology and Dynamics. *Proc. Natl. Acad. Sci. U. S. A.* **2013**, *110* (33), E3054.
- (18) Gong, K.; Feng, S.-S.; Go, M. L.; Soew, P. H. Effects of PH on the Stability and Compressibility of DPPC/Cholesterol Monolayers at the Air–Water Interface. *Colloids Surf., A* **2002**, 207 (1–3), 113–125.
- (19) Sapia, P.; Coppola, L.; Ranieri, G.; Sportelli, L. Effects of High Electrolyte Concentration on DPPC-Multilayers: An ESR and DSC Investigation. *Colloid Polym. Sci.* 1994, 272 (10), 1289–1294.
- (20) Binks, B. P. Colloidal Particles at a Range of Fluid-Fluid Interfaces. *Langmuir* **2017**, 33 (28), 6947–6963.
- (21) Lin, W.-H.; Chen, T.-H.; Chang, J.-K.; Taur, J.-I.; Lo, Y.-Y.; Lee, W.-L.; Chang, C.-S.; Su, W.-B.; Wu, C.-I. A Direct and Polymer-Free Method for Transferring Graphene Grown by Chemical Vapor Deposition to Any Substrate. *ACS Nano* **2014**, *8* (2), 1784–1791.
- (22) Goggin, D. M.; Samaniuk, J. R. 2D Colloids: Size- and Shape-Controlled 2D Materials at Fluid-Fluid Interfaces. *Langmuir* **2021**, 37 (48), 14157–14166.
- (23) Kim, C.; Yoon, M.-A.; Jang, B.; Kim, H.-D.; Kim, J.-H.; Hoang, A. T.; Ahn, J.-H.; Jung, H.-J.; Lee, H.-J.; Kim, K.-S. Damage-Free Transfer Mechanics of 2-Dimensional Materials: Competition

- between Adhesion Instability and Tensile Strain. NPG Asia Mater. 2021, 13 (1), 44.
- (24) Vandebril, S.; Franck, A.; Fuller, G. G.; Moldenaers, P.; Vermant, J. A Double Wall-Ring Geometry for Interfacial Shear Rheometry. *Rheol. Acta* **2010**, *49* (2), 131–144.
- (25) Kim, K.; Choi, S. Q.; Zasadzinski, J. A.; Squires, T. M. Nonlinear Chiral Rheology of Phospholipid Monolayers. *Soft Matter* **2018**, *14* (13), 2476–2483.
- (26) Blair, V. E. Functional Particle Interfaces and Their Fabrication, Doctoral Dissertation, ETH Zurich, 2018; p. 135.
- (27) Kale, S. K.; Cope, A. J.; Goggin, D. M.; Samaniuk, J. R. A Miniaturized Radial Langmuir Trough for Simultaneous Dilatational Deformation and Interfacial Microscopy. *J. Colloid Interface Sci.* **2021**, 582, 1085–1098.
- (28) Gingell, D.; Todd, I. Interference Reflection Microscopy. A Quantitative Theory for Image Interpretation and Its Application to Cell-Substratum Separation Measurement. *Biophys. J.* **1979**, *26* (3), 507–526.
- (29) Goggin, D. M.; Zhang, H.; Miller, E. M.; Samaniuk, J. R. Interference Provides Clarity: Direct Observation of 2D Materials at Fluid–Fluid Interfaces. *ACS Nano* **2020**, *14* (1), 777–790.
- (30) Limozin, L.; Sengupta, K. Quantitative Reflection Interference Contrast Microscopy (RICM) in Soft Matter and Cell Adhesion. *Chem. Eur. J. Chem. Phys.* **2009**, *10* (16), 2752–2768.
- (31) Reddy, K. A.; Doraiswamy, L. K. Estimating Liquid Diffusivity. *Ind. Eng. Chem. Fundam.* **1967**, 6 (1), 77–79.
- (32) Bosma, J. C.; Wesselingh, J. A. Estimation of Diffusion Coefficients in Dilute Liquid Mixtures. *Chem. Eng. Res. Des.* **1999**, 77 (4), 325–328.
- (33) Danov, K. D.; Kralchevsky, P. A. Capillary Forces between Particles at a Liquid Interface: General Theoretical Approach and Interactions between Capillary Multipoles. *Adv. Colloid Interface Sci.* **2010**, *154* (1–2), 91–103.
- (34) Kralchevsky, P. A.; Nagayama, K. Capillary Interactions between Particles Bound to Interfaces, Liquid Films and Biomembranes. *Adv. Colloid Interface Sci.* **2000**, 85 (2–3), 145–192.
- (35) Velev, O. D.; Denkov, N. D.; Paunov, V. N.; Kralchevsky, P. A.; Nagayama, K. Direct Measurement of Lateral Capillary Forces. *Langmuir* **1993**, *9* (12), 3702–3709.
- (36) Vella, D.; Mahadevan, L. The "Cheerios Effect. Am. J. Physics 2005, 73 (9), 817–825.
- (37) Wei, Y.; Wang, B.; Wu, J.; Yang, R.; Dunn, M. L. Bending Rigidity and Gaussian Bending Stiffness of Single-Layered Graphene. *Nano Lett.* **2013**, *13* (1), 26–30.
- (38) Lu, Q.; Arroyo, M.; Huang, R. Elastic Bending Modulus of Monolayer Graphene. J. Phys. D: Appl. Phys. 2009, 42 (10), No. 102002.
- (39) Goggin, D. M.; Bei, R.; Anderson, R.; Gómez-Gualdrón, D. A.; Samaniuk, J. R. Stacking of Monolayer Graphene Particles at a Water-Vapor Interface. *J. Phys. Chem. C* **2021**, *125* (14), 7880–7888.